

# An actin bracket-induced elastoplastic transition determines epithelial folding irreversibility

Received: 25 February 2024

Accepted: 25 November 2024

Published online: 12 December 2024

Aki Teranishi<sup>1</sup>, Misato Mori<sup>2</sup>, Rihoko Ichiki<sup>1</sup>, Satoshi Toda<sup>2</sup>, Go Shioi<sup>3</sup> & Satoru Okuda<sup>2,4</sup>✉

During morphogenesis, epithelial sheets undergo sequential folding to form three-dimensional organ structures. The resulting folds are often irreversible, ensuring that morphogenesis progresses in one direction. However, the mechanism establishing folding irreversibility remains unclear. Here, we report a mechanical property of epithelia that determines folding irreversibility. Using a mechanical assay, we demonstrate that long-term, high-curvature folding induces plastic, irreversible deformations, while short-term or low-curvature folding results in an elastic, shape-restoring response. This elastic-plastic transition occurs in a switch-like manner, with critical thresholds in folding curvature and duration. The transition is induced by F-actin accumulating into a bracket-like structure across the fold, triggered by cells sensing deformations via mechanosensitive signaling pathways, including TRPC 3/6-mediated calcium influx and ligand-independent EGFR activation. These results demonstrate that cells control epithelial folding irreversibility by detecting folding characteristics and adaptively switching between elastic and plastic responses, providing mechanical insight into the directionality of morphogenesis.

Morphogenesis proceeds in one direction, with sequential epithelial folds transforming planar sheets into three-dimensional structures. Importantly, each fold is irreversible, and this irreversibility is essential for the formation of complex organ structures. Morphogenesis cannot proceed if the folds return to their original shapes; therefore, ensuring the irreversibility of epithelial folding is fundamental for achieving morphogenesis.

Various cellular behaviors that generate mechanical forces, including apical constriction, serve as key drivers of epithelial folding<sup>1–5</sup>. The balance between these forces and mechanical properties, such as elasticity and viscosity, determines the amount and rate of tissue deformations<sup>6–10</sup>. However, folding irreversibility cannot be explained by either driving forces or viscoelastic properties. Because the epithelium is constantly exposed to various deformations by the

activities of its constituent cells and surrounding tissues<sup>11–13</sup>, successful morphogenesis requires epithelia to retain necessary deformations while resisting unnecessary deformations.

We previously demonstrated that the epithelium undergoes plastic bending, facilitating retinal invagination in a mechanosensitive manner<sup>14</sup>. Additionally, recent studies examining tissue fluidization<sup>15–17</sup> and viscoelasticity<sup>9,18,19</sup> have, either implicitly or explicitly, described plastic deformations. In contrast, the epithelium exhibits bending elasticity, which allows it to resist external forces<sup>20–22</sup>. Cells respond mechanosensitively to imposed deformations<sup>23–26</sup> and surrounding curvatures<sup>27–29</sup>, indicating that cells may regulate their bending elasticity and plasticity—properties that confer opposing responses to external forces—to control the irreversibility of epithelial folding. However, although the importance of mechanical plasticity is

<sup>1</sup>Division of Nano Life Science, Graduate School of Frontier Science Initiative, Kanazawa University, Kanazawa, Japan. <sup>2</sup>Nano Life Science Institute, Kanazawa University, Kanazawa, Japan. <sup>3</sup>RIKEN Center for Biosystems Dynamics Research, Kobe, Japan. <sup>4</sup>Sapiens Life Sciences, Evolution and Medicine Research Center, Kanazawa University, Kanazawa, Japan. ✉e-mail: [satokuda@staff.kanazawa-u.ac.jp](mailto:satokuda@staff.kanazawa-u.ac.jp)

increasingly recognized<sup>30</sup>, the elastoplastic property of epithelial folding and its regulatory mechanisms remain poorly understood.

We developed a mechanical indentation assay for measuring the elastoplastic properties of the epithelium. We observed both elastic and plastic responses in several types of epithelia, including a mouse embryonic optic vesicle (OV), mouse embryonic stem cell (mESC)-derived OV organoid, and Madin–Darby canine kidney (MDCK) cell-derived cyst. Further experiments using the MDCK cell-derived cyst revealed an elastoplastic transition and its underlying molecular mechanisms, which likely serve to adaptively control the irreversibility of the epithelial folding response through the detection of imposed deformation.

## Results

### Epithelial response switches between elastic and plastic depending on folding duration and curvature

To measure epithelial bending plasticity, we developed an indentation assay, in which a glass pipette is used to indent the epithelium, forming a single fold. After holding the pipette in place for a defined time, the pipette is removed to relax the residual strain (Fig. 1a, b and Supplementary Fig. 1a–e). The bending plasticity was assessed based on the tissue shape 5 min after removing the pipette; within this time the residual strain had fully relaxed (Supplementary Fig. 1c). This assay enables the assessment of bending properties as a function of the hold duration ( $\tau$ ) and curvature ( $\kappa$ ).

We first assessed the dependence of the bending property on  $\tau$ . Mouse embryonic OV tissue exhibited an elastoplastic response dependent on  $\tau$ : when  $\tau = 20$  s, the tissue restored its original shape, whereas the tissue deformed irreversibly when  $\tau = 30$  min (Fig. 1c and Video S1). A similar response was observed in mESC-derived OV organoids (Fig. 1d and Video S1), indicating that this elastoplastic response is an intrinsic property of OVs, independent of surrounding tissues, such as the epidermis or the periocular mesenchyme. MDCK cell-derived cysts displayed a similar elastoplastic response (Fig. 1e and Video S1), suggesting that this response is not specific to mouse optic vesicles but is likely a general characteristic of many types of epithelia, including embryonic and cultured tissues. The plastic deformation that occurred after the 30-min indentation was maintained for several hours after unloading (Supplementary Fig. 1b, c, f).

In experiments using  $\tau = 30$  min, the tissue exhibited springback, in which a slight return to the original shape was observed after retraction, indicating a mixed elastic and plastic response. To quantify this mixed response, we introduced the degree of bending plastic ratio,  $\psi$ , based on the epithelial curvature measured at the fold caused by the indentation (see “Methods” section). This criterion represents the contribution of plastic deformation to total deformation. Significant differences were observed between the elastic and plastic responses among embryonic OV tissues, mESC-derived OV organoids, and MDCK cell-derived cysts (Fig. 1f).

We performed further quantitative analyses using MDCK cell-derived cysts, which have consistent sizes and shapes and no surrounding tissues. The measurements revealed that  $\psi$  is dependent on  $\tau$  and  $\kappa$ , with increases in  $\tau$  and  $\kappa$  associated with a monotonic increase in  $\psi$ , from elastic to plastic (Fig. 1g, h). The rate of increase in  $\psi$  is nonlinear, with a switch-like transition observed at certain  $\tau$  and  $\kappa$  values. By fitting a sigmoidal function, we identified the critical duration as  $\tau_{ct} = 13$  min and the critical curvature as  $\kappa_{ct} = 0.126 \mu\text{m}^{-1}$ . The original shape tended to be restored when  $\tau$  was below either  $\tau_{ct}$  or  $\kappa_{ct}$ , whereas the tissue deformed irreversibly when  $\tau$  was above  $\tau_{ct}$  and  $\kappa_{ct}$ . These results show that the epithelium switches its bending response bistably between elastic and plastic depending on the characteristics of the imposed deformation.

We addressed the effects of luminal pressure on the elastoplastic response by measuring the entire cyst and luminal volumes. The measurements revealed that both the cyst and luminal volumes

remained constant during indentation (Supplementary Fig. 2a, b), suggesting that the luminal pressure does not contribute to the plastic response. Moreover, we punctured the cyst with a glass pipette and found that the cyst volume shrank immediately upon puncture (Supplementary Fig. 2c, d), indicating that the cyst has a luminal pressure, which may contribute to the elastic response. Furthermore, to clarify that the elastoplastic response is caused by the cyst itself, we measured the viscoelastic properties of Matrigel, which sustains the cyst during indentation. Matrigel has a stiffness (12 Pa) much lower than that of the cyst and a relaxation time (3.8 s) much shorter than the transition time ( $\kappa_{ct} = 13$  min) (Supplementary Fig. 2e–g). These results demonstrate that the elastoplastic response originates from the cyst itself.

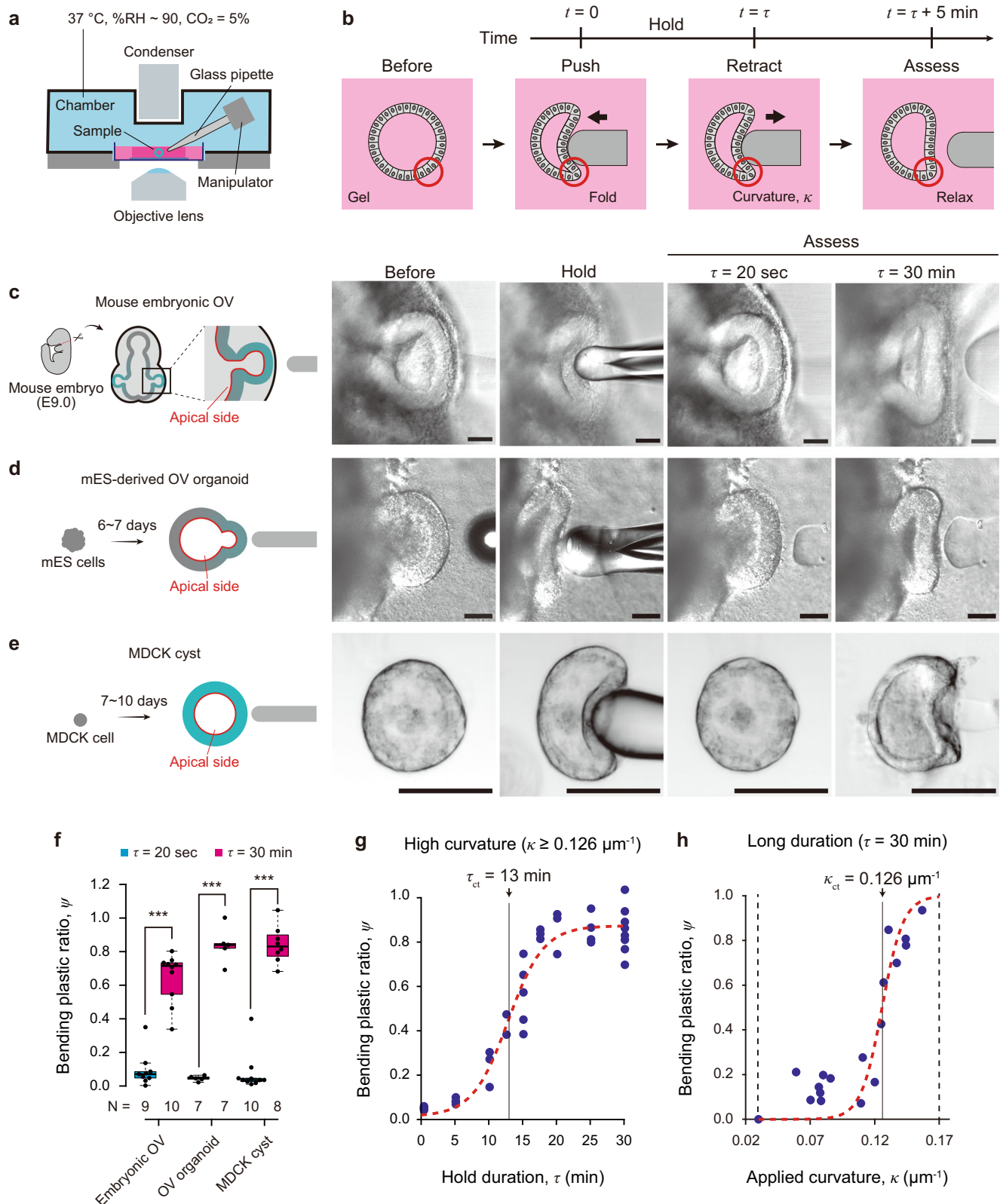
To understand the switch-like elastoplastic transition from a theoretical viewpoint, we developed a simple mathematical model for the cyst properties (Supplementary Fig. 3a, b). The model describes the epithelial property using an extended standard solid body model<sup>31</sup>, characterized by a series of spring, Kelvin, and Bingham elements with a yield delay. This model successfully recapitulated the elastoplastic response of the epithelium, exhibiting switch-like transitions from elastic to plastic with certain duration and curvature thresholds (Supplementary Fig. 3c). In contrast, the transitions could not be observed when removing either the plasticity (Supplementary Fig. 3d) or the delay (Supplementary Fig. 3e). These results demonstrate that the elastoplastic property with a yield delay induces the switch-like transitions of the epithelium depending on both the duration and curvature.

### Epithelial folding triggers ligand-free activation of epidermal growth factor receptor (EGFR) and downstream PI3K–Akt pathway

To address how cells sense deformation, we first focused on EGFR, which plays the role of a mechanosensor in epithelial tissues<sup>32,33</sup>. To address the role of EGFR in the elastoplastic property, we measured  $\psi$  after the application of inhibitors. During indentation, EGFR becomes activated in a mechanosensitive manner, and the inhibitors PD153035, LY294002, and ipatasertib, which inhibit EGFR, phosphoinositide 3-kinase (PI3K), and Akt, respectively, all suppressed the elastoplastic transition (Fig. 2a and Supplementary Fig. 4a), indicating that the EGFR–PI3K–Akt pathway regulates the transition.

The mitogen-activated protein kinase kinase (MEK) inhibitor PD0325901 did not affect the elastoplastic transition (Fig. 2a), indicating that the MEK–ERK pathway is not involved in the transition. However, the deformation activated extracellular signal-related kinase (ERK), and this ERK activity was inhibited by EGFR inhibitor PD153035 (Fig. 2d, f and Supplementary Fig. 4b, c), indicating that ERK activation occurred through EGFR. Therefore, to monitor the EGFR activation in the transition, we utilized a Förster resonance energy transfer (FRET) sensor for ERK activation (Fig. 2b, Supplementary Fig. 4b, and Video S2). The FRET ratio increased rapidly within the first 5 min of indentation, particularly near the fold (Fig. 2b, c), followed by a gradual decrease (Fig. 2d).

To further investigate what triggers EGFR activation, we assessed cysts derived from MDCK cells engineered to knockout all endogenous EGFR ligands: epidermal growth factor (EGF), transforming growth factor alpha (TGF $\alpha$ ), heparin-binding EGF-like growth factor (HBEGF), and epiregulin (EREG)<sup>34</sup>. These cysts displayed an increased FRET ratio and elastoplastic transition in response to deformation (Fig. 2e, f and Supplementary Fig. 4d, e), and similar results were obtained in cysts derived from MDCK cells engineered to knockout only EGF and those engineered to knockout disintegrin and metalloprotease 17 (ADAM17), in which TGF $\alpha$ , HBEGF, and EREG are inactivated (Fig. 2e, f and Supplementary Fig. 4d, e). Moreover, the FRET ratio was not increased by low-



curvature folding (Fig. 2f and Supplementary Fig. 4d, e). These results show that cells sense the curvature of folding, and substantial folding triggers EGFR activity in a ligand-independent manner.

To elucidate the trigger of EGFR activation, we focused on adherens junctions, which interact with EGFR and modulate its downstream signaling pathways, including the PI3k–Akt pathway<sup>35,36</sup>. We examined cysts derived from MDCK cells engineered to knockout  $\alpha$ -catenin.

These cysts did not exhibit an increased FRET ratio or elastoplastic transition in response to deformation (Fig. 2e, f and Supplementary Fig. 4d, e), indicating that adherens junctions are required for EGFR activation and the subsequent elastoplastic transition.

Our findings indicate that the elastoplastic transition involves the mechanosensitive and ligand-independent activation of the EGFR–PI3K–Akt pathway, which is consistent with previous reports

**Fig. 1 | Epithelial response switches between elastic and plastic depending on folding duration and curvature.** **a** Mechanical indentation device with a custom culture chamber on a confocal microscope. An electric piezo manipulator with a glass pipette is placed inside. **b** Schematic for the flow of the indentation assay. Bending plastic ratio,  $\psi$ , was introduced, and its dependence on the hold duration,  $\tau$ , was explored. **c–e** Schematics and images of the epithelium before, during, and after indentation for **c** mouse embryonic optic vesicles (OVs) at E9.0. **d** An OV organoid derived from mouse embryonic stem cells (mESCs) at days 6 or 7, and **e** a cyst derived from Madin–Darby canine kidney (MDCK) cells. More than seven experiments were repeated independently for each type of epithelium. Scale bar,

50  $\mu\text{m}$ . **f** Bending plastic ratio,  $\psi$ , of three types of epithelia: mouse embryonic OVs ( $p = 5.51\text{e} - 8$ ), OV organoid derived from mESCs ( $p = 3.34\text{e} - 8$ ), and MDCK cysts ( $p = 2.75\text{e} - 10$ ). Box plots in **(f)**: center: median; bounds, 25th and 75th percentiles; whiskers, min, and max; \*\*\* $P < 0.001$  (two-sided Welch's  $t$ -test).  $N$  indicates a biologically independent sample. **g, h** Bending plastic ratio,  $\psi$ , of MDCK cell-derived cysts as a function of hold duration  $\tau$  and applied curvature  $\kappa$ , respectively. The red dotted line shows sigmoid functions fitted by the least squares method, in which the critical duration,  $\tau_{ct}$  is 13 min and  $\kappa_{ct}$  is  $0.126 \mu\text{m}^{-1}$ , respectively. Source data are provided as a Source Data file.

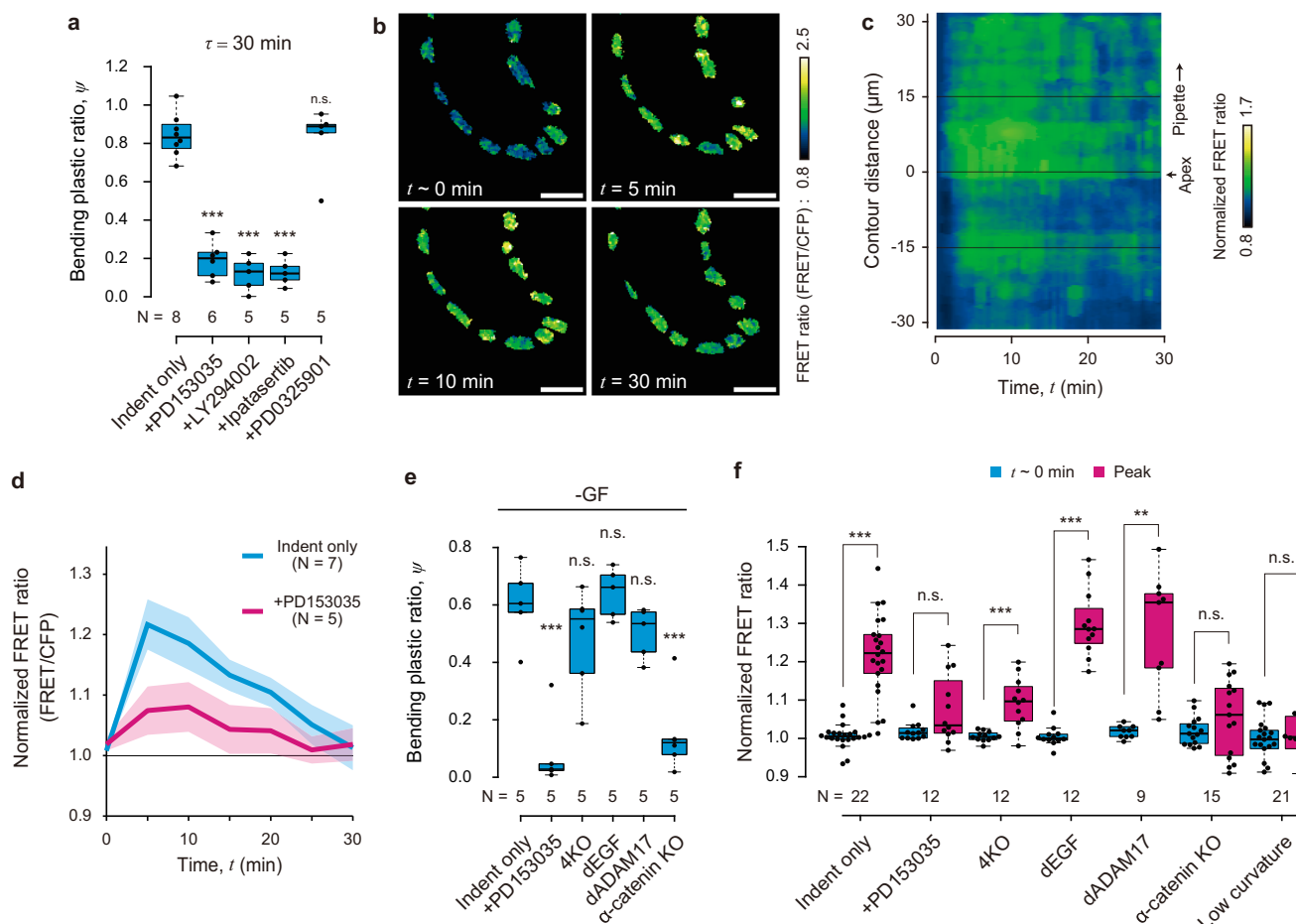


**Fig. 2 | Epithelial folding triggers ligand-free activation of EGFR and downstream PI3K–Akt pathway.** **a** Bending plastic ratio,  $\psi$ , under drug treatment conditions targeting EGFR or downstream molecules inhibitions. The conditions included treatment with PD153035 ( $p = 5.75\text{e} - 8$ ), LY294002 ( $p = 1.30\text{e} - 7$ ), Ipatasertib ( $p = 1.91\text{e} - 8$ ), and PD0325901 ( $p = 0.810$ ) for  $\tau = 30$  min.  $N$  indicates a biologically independent sample. **b** ERK-FRET images for indentation only immediately after initiation, at the time of peak ratio, and 30 min after indentation. Eight experiments were repeated independently. Scale bars, 15  $\mu\text{m}$ . **c** Kymograph of ERK-FRET ratio along the epithelium contour over time under conditions of indentation only. FRET ratio at each pixel is normalized to its value immediately after indentation and averaged across samples ( $N = 5$ ). The pipette is at a positive distance from the apex with the highest curvature. **d** Time variations of ERK-FRET ratios around the apex during indentation for indentation only and indentation in the presence of EGFR inhibition ( $N = 5$  biological replicates). Data represent the mean  $\pm$  s.e. **e** Bending plastic ratio,  $\psi$ , under drug treatment conditions and the knockout of EGFR agonists excluding growth factors in the medium. The conditions included treatments with PD153035 ( $p = 2.80\text{e} - 4$ ), the knockout of all four

growth factors (4KO,  $p = 0.149$ ), EGF (dEGF,  $p = 0.202$ ), a factor upstream of the other three agonists (dADAM17,  $p = 0.612$ ), and the knockout of  $\alpha$ -catenin ( $\alpha$ -catenin KO,  $p = 0.00116$ ) for  $\tau = 30$  min.  $N$  indicates a biologically independent sample. **f** ERK-FRET ratios of individual cells under drug treatment conditions and the knockout of EGFR agonists, as well as under a condition of low-curvature folding. The conditions included indentation only ( $p = 2.74\text{e} - 9$ ), treatment with PD153035 ( $p = 0.0583$ ), the knockout of all four growth factors (4KO,  $p = 7.68\text{e} - 4$ ), EGF ( $p = 4.43\text{e} - 8$ ), ADAM17 ( $p = 0.00106$ ),  $\alpha$ -catenin ( $p = 0.218$ ), and low-curvature folding ( $p = 0.232$ ) at  $t = 0$  min, and the time of the peak ratio.  $N$  indicates the number of cells. More than five biological replicates. Box plots in **(a)**, **(e)**, and **(f)**: center, median; bounds, 25th and 75th percentiles; whiskers, min, and max; \*\* $P < 0.01$  and \*\*\* $P < 0.001$  (two-sided Welch's  $t$ -test). ADAM17 is a disintegrin and metalloproteinase 17, EGF epidermal growth factor, EGFR epidermal growth factor receptor, ERK extracellular signal-related kinase, FRET Förster resonance energy transfer, PI3K phosphoinositide 3-kinase. Source data are provided as a Source Data file.



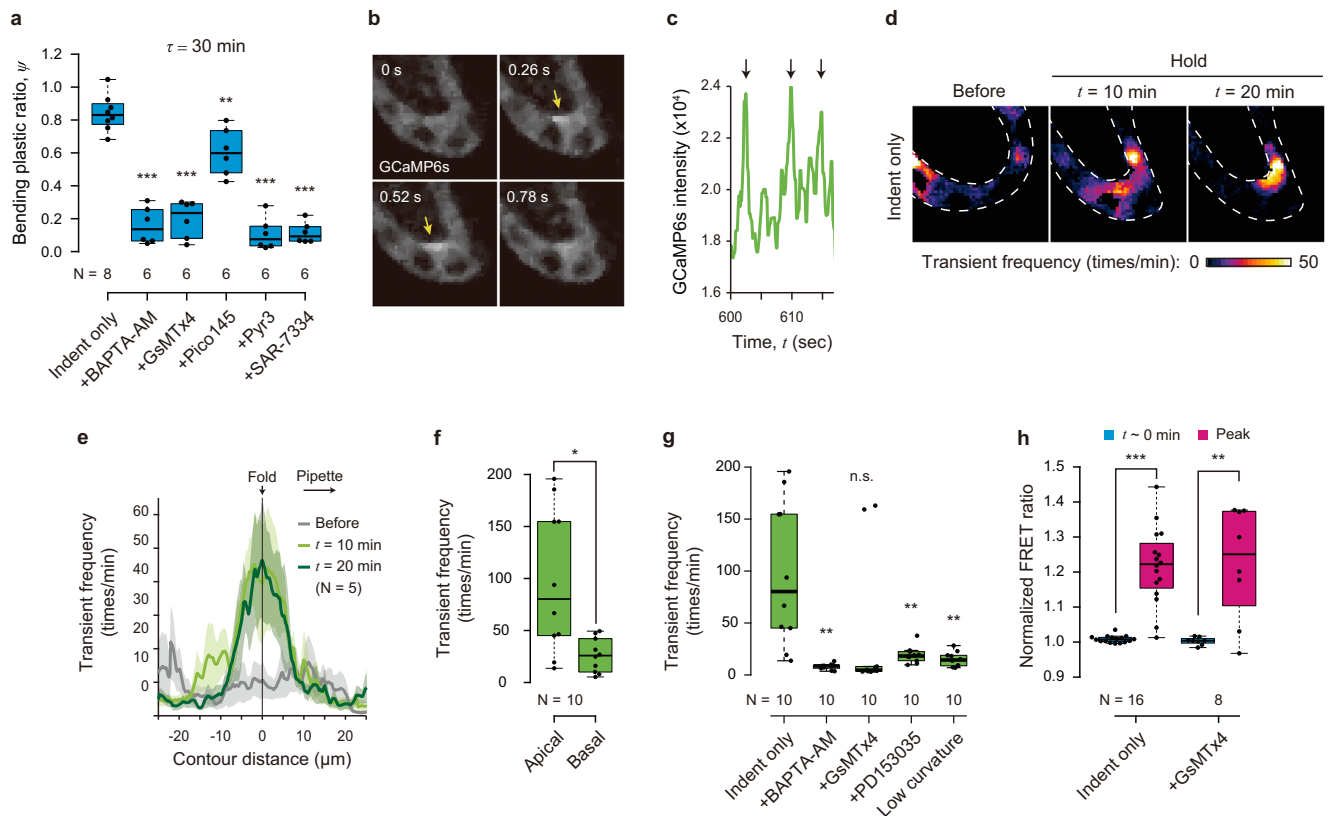


**Fig. 3 | TRPC3/6-mediated mechanosensing triggers calcium transient at the epithelial fold under EGFR activation.** **a** Bending plastic ratio,  $\psi$ , for  $\tau = 30$  min under drug treatment conditions targeting intracellular calcium chelation, and mechanosensitive channel inhibition. The conditions included treatments with BAPTA-AM ( $p = 2.11e - 7$ ), GsMTx4 ( $p = 5.28e - 7$ ), Pico145 ( $p = 0.00856$ ), Pyr3 ( $p = 2.70e - 8$ ), and SAR7334 ( $p = 5.15e - 9$ ). **b** Time-lapse images of GCaMP6s 10 min after indentation initiation. Calcium transients occurred in the apical region (arrows). Five experiments were repeated independently. **c** Time variations of calcium concentrations around the apex 10 min after indentation initiation. **d, e** Spatial distributions of calcium transient frequency: before, 10 min, and 20 min after indentation initiation. Map view (**d**) and distribution along the epithelium contour averaged across samples (**e**). Dotted lines indicate epithelium contours. Data represent the mean  $\pm$  s.e. ( $N = 5$ ). **f** Calcium transient frequency at apical and

basal regions ( $N = 5$  biological replicates,  $p = 0.0101$ ). **g** Calcium transient frequency around the apex under drug treatment conditions targeting intracellular calcium chelation, mechanosensitive channel inhibition, and EGFR inhibition, as well as under a condition of low-curvature folding. The conditions included BAPTA-AM ( $p = 0.00277$ ), GsMTx4 ( $p = 0.0574$ ), PD153035 ( $p = 0.00601$ ), and low-curvature folding ( $p = 0.00445$ ). **h** ERK-FRET ratios of individual cells for indentation only ( $p = 1.56e - 9$ ) and in the presence of mechanosensitive channel inhibitor, GsMTx4 ( $p = 0.00568$ ) at  $t = 0$  and the time of peak ratio. Box plots in (**a**) and (**e–h**): center, median; bounds, 25th and 75th percentiles; whiskers, min, and max; \* $P < 0.05$ , \*\* $P < 0.01$ , \*\*\* $P < 0.001$  (two-sided Welch's  $t$ -test).  $N$  indicates a biologically independent sample. EGFR epidermal growth factor receptor, ERK extracellular signal-related kinase, FRET Förster resonance energy transfer, TRPC transient receptor potential canonical. Source data are provided as a Source Data file.

that EGFR is activated without a ligand<sup>37–39</sup> and in a mechanosensitive manner<sup>40–42</sup>. Furthermore, our results highlight the crucial role of adherens junctions, which is consistent with previous reports indicating that mechanical forces facilitate EGFR activation via adherens junctions<sup>33,43</sup>, promoting PI3k activation<sup>43</sup>.

### TRPC3/6-mediated mechanosensing triggers calcium transients at the epithelial fold under EGFR activation

Our inhibitor assays revealed that mechanosensitive calcium channels are required for elastoplastic transition. The transition was suppressed by the inhibition of mechanosensitive cation channels, including transient receptor potential canonical (TRPC)1/6, using Grammostola mechanotoxin 4 (GsMTx4)<sup>44,45</sup>, and by the chelation of intracellular calcium, using BAPTA-AM (Fig. 3a and Supplementary Fig. 5a). Specifically, the transition was suppressed by the inhibition of TRPC6 with SAR-7334; however, it still occurred even under the inhibition of TRPC1 with Pico145 (Fig. 3a), indicating that TRPC6-mediated calcium influx is necessary for the transition. Moreover, TRPC3 and TRPC6 form a heteromeric complex on the apical side<sup>46</sup>, and inhibition of TRPC3 with Pyr3 suppressed the transition (Fig. 3a), suggesting that cells detect deformation via TRPC3/6-mediated calcium influx on the apical side.

We performed live intracellular calcium imaging to observe the spatial pattern of calcium influx using cysts derived from a cell line stably expressing the calcium indicator GCaMP6s. We found that indentation induced typical calcium transients (Fig. 3b, c, Supplementary Fig. 5b, and Video S3) that were maintained throughout the indentation duration. These transients were specifically localized at the apical side of the fold (Fig. 3d–f) in a region measuring  $-20.7 \mu\text{m}$  long along the contour and  $-5.0 \mu\text{m}$  thick along the apicobasal axis (Supplementary Fig. 5c–g). These transients were suppressed by GsMTx4 and BAPTA-AM (Fig. 3g and Supplementary Fig. 5c, d), which corresponds to the suppression of the transition by these inhibitors (Fig. 3a). Moreover, these transients were not triggered by low-curvature folding (Fig. 3g and Supplementary Fig. 5c, d). These findings show that cells detect the folding curvature on the apical side via mechanosensitive calcium influx.

We also assessed the interaction between EGFR activation and calcium influx. To clarify whether EGFR activation affects calcium signaling, we performed live calcium imaging of cysts derived from GCaMP6s-expressing cells treated with the EGFR inhibitor PD153035, which revealed that PD153035 suppressed chronic calcium transients (Fig. 3g and Supplementary Fig. 5c, d). By contrast, we observed increased FRET in response to indentation in the presence of the

mechanosensitive channel inhibitor GsMTx4 (Fig. 3h and Supplementary Fig. 4d, e). These results indicate that the elastoplastic transition requires both mechanosensitive pathways: EGFR activation and calcium influx. While both of them are independently triggered by deformation, calcium influx is triggered under EGFR activation. Through the calcium pathway, cells detect apical deformation.

### Actin bracket formation establishes elastoplastic transition with a tunable critical duration

To elucidate the mechanism that establishes the transition, we performed live imaging of F-actin using cysts derived from an MDCK cell line, stably expressing mCherry-fused Lifeact. During indentation, F-actin gradually accumulated locally at the apical side of the fold (Fig. 4a, Supplementary Fig. 6a, and Video S4). Three-dimensional imaging revealed F-actin accumulation not only on the apical side but also along the lateral boundaries between cells (Fig. 4b and Video S5). F-actin accumulated to form a bracket-like structure along the apical side of the epithelium, which we term the ‘actin bracket,’ ~9.6  $\mu\text{m}$  long and 2.0  $\mu\text{m}$  thick (Fig. 4c, d and Supplementary Fig. 6b–e), corresponding to the region with frequent calcium transients (Supplementary Fig. 5e–g). This correlation was further confirmed by the simultaneous observation of F-actin and calcium (Supplementary Fig. 6f–h).

F-actin accumulation occurred most rapidly at the point of highest curvature, showing a linear increase for the first 10 min and then plateauing (Fig. 4e). This time duration is shorter than the critical duration for the elastoplastic transition (Fig. 1g). The region of accumulation gradually expanded from this point, taking ~16 min to fully form the actin bracket and cover the fold (Fig. 4e). This time duration corresponds to the critical duration of the transition (Fig. 1g), indicating that the formation of the actin bracket is essential for the transition.

To clarify the role of F-actin accumulation in the elastoplastic transition, we measured  $\psi$  following the inhibition of F-actin polymerization with cytochalasin D, latrunculin A, or CK-666 (Fig. 4f, g and Supplementary Fig. 7a). These inhibitors not only suppressed F-actin accumulation but also inhibited the transition, indicating the critical role of F-actin polymerization. In addition, inhibiting the EGFR–PI3K–Akt and calcium pathways, which are known regulators of F-actin dynamics<sup>47–51</sup>, also halted both F-actin accumulation and the transition (Figs. 2a, 3a, 4g and Supplementary Fig. 7c). By contrast, inhibiting MEK or TRPC1 did not affect F-actin accumulation, corresponding to the lack of effect on the transition. Moreover, this F-actin accumulation was not induced by low-curvature folding (Fig. 4f and Supplementary Fig. 7c). These results indicate that F-actin accumulation, which is regulated downstream of the EGFR–PI3K–Akt and calcium pathways triggered by substantial folding, is essential for the elastoplastic transition.

Interestingly, enhancing actin polymerization with jasplakinolide resulted in a plastic response as rapidly as 5 min after indentation (Fig. 4f, g and Supplementary Fig. 7b). Even in the presence of jasplakinolide, short-term indentations induced elastic responses, but the critical duration required for the elastoplastic transition ( $\tau_{\text{ct}} = 2.8$  min) was significantly shorter than under untreated conditions (Fig. 4h). This result indicates that the actin polymerization rate determines the critical duration required for elastoplastic transition.

Finally, we demonstrated that local F-actin accumulation, specifically actin bracket formation, rather than F-actin throughout the entire tissue establishes the elastoplastic transition. We conducted an indentation assay combined with a local pharmacological intervention using two pipettes (Fig. 4i); one applied an indentation in the tissue, whereas the other released inhibitors in a specific local region around the tissue. Inhibition of local F-actin polymerization at the fold prevented actin bracket formation and the following elastoplastic

transition, whereas inhibition of polymerization in regions away from the fold did not have this effect (Fig. 4j–l). These results confirm that a locally formed actin bracket at the fold plays a role in establishing the elastoplastic transition of the epithelium.

These results show that F-actin accumulates across the fold, forming a bracket-like structure that establishes elastoplastic transition, and that the critical duration can be tuned by adjusting the actin polymerization rate.

### Discussion

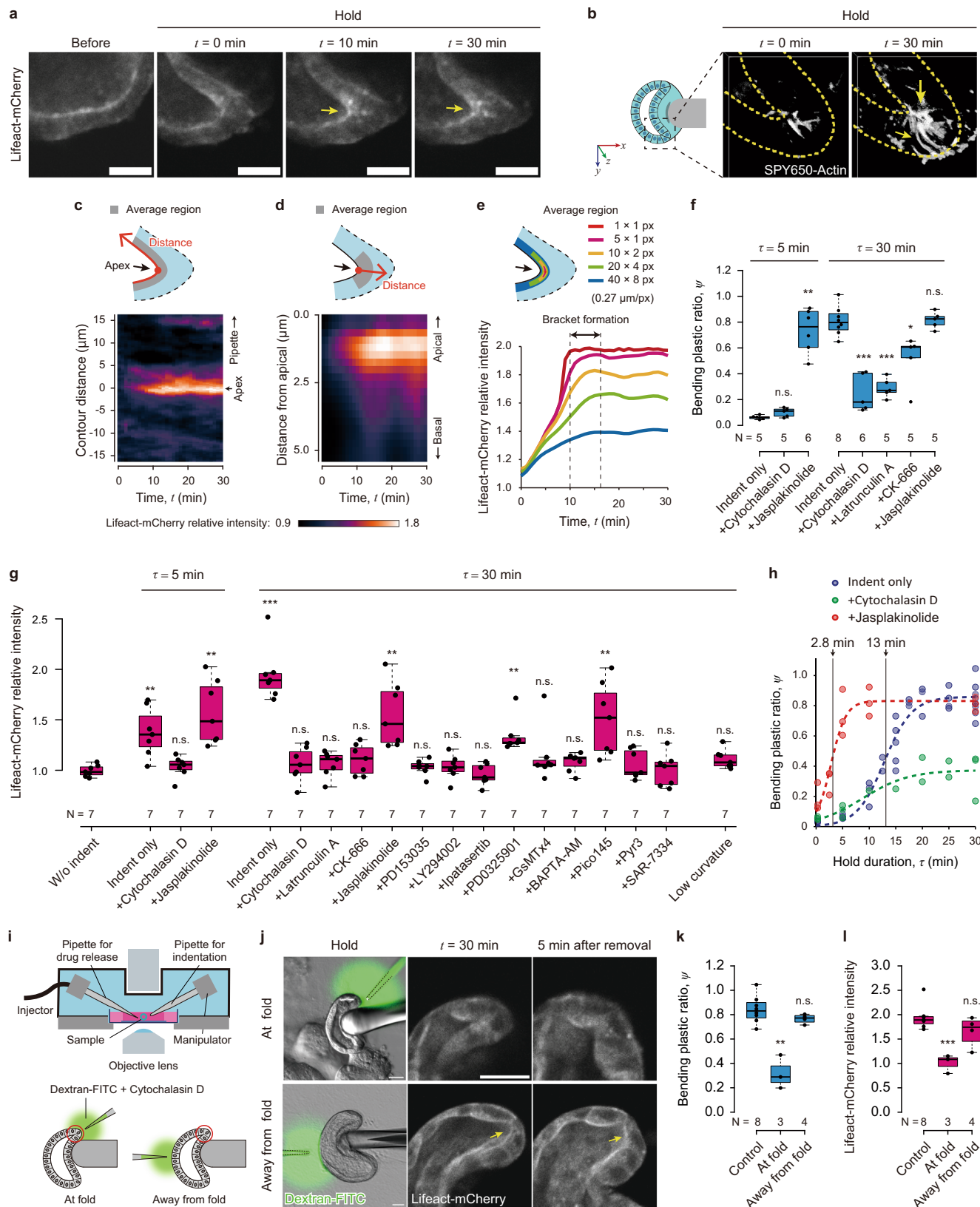
In this study, we elucidated a mechanism underlying elastoplastic transition during epithelial folding, which occurs as a switch-like response that is dependent on the curvature and duration of the imposed deformation. The transition is established by the accumulation of F-actin in response to mechanosensing pathway activation (Fig. 5).

The concept of elastoplastic transition is well-known in the field of solid materials engineering. However, its mechanics in epithelial folding have not been previously reported, to our knowledge. Metals and resins typically exhibit strain-dependent elastoplastic transitions, with plastic deformation resulting from large deformations<sup>52</sup>. By contrast, elastoplastic transitions for fabrics and other materials are often time-dependent transitions, with the transition duration dependent on the material and environment. Transitions in these materials are generally caused by passive mechanisms, such as atomic displacement in metals, crystal exfoliation in resins, and fiber displacement in fabrics (Supplementary Fig. 8a). The tunable critical duration in epithelial folding, as regulated by living cells, represents a sharp contrast with the transition mechanics associated with other materials.

The elastoplastic transition of the epithelium is analogous to tissue fluidization<sup>16,17,53,54</sup>, as both of these processes are able to induce irreversible deformation within the epithelial plane (Supplementary Fig. 8b). However, fluidization requires a phase transition of the tissue from a solid to a liquid, whereas tissue remains in the solid phase during the elastoplastic transition. Kinematically, fluidization is caused by a global rearrangement of cells at the tissue scale<sup>16,17,53,54</sup>, and plastic elongation within the epithelial plane requires F-actin remodeling at this scale<sup>55</sup>. In contrast, the elastoplastic transition in epithelial folding is caused by a change in local cell behavior and does not require global rearrangement. In the elastoplastic transition, local cell behavior alone can cause tissue-scale deformation, generating an irreversible fold structure.

The cells that drive apical constriction in epithelial folding may also undergo elastoplastic transition, responding to their own deformation (Supplementary Fig. 8c). This idea is supported by observations that elastoplastic transition and apical constriction share several key components, including actomyosin activity<sup>1–3,14,56–59</sup>, calcium signaling<sup>14,57</sup>, and EGFR activation<sup>58–60</sup>. Apical constriction occurs collectively for all cells within a specific region and period; however, individual cells are constantly generating relatively short-term forces through behaviors such as division, apoptosis, and contraction, which can introduce noise<sup>54,61</sup>. Elastoplastic transition may play a key role in stabilizing appropriate invaginations, filtering out the noise from short-term individual cell forces, and enabling collective cellular behaviors.

The elastoplastic transition of the epithelium may play a crucial role in embryogenesis, such as in mouse optic cup formation. During this process, the neuroepithelium forms a hemispherical OV, in which the distal part differentiates into the neural retina (NR) and invaginates into the surrounding retinal pigment epithelium (RPE), forming a cup-like shape. We previously demonstrated that this NR invagination occurs due to the bending force generated by the NR itself<sup>4</sup>. This bending force creates a fold at the boundary between the NR and the adjacent RPE, inducing calcium signaling, actomyosin constriction, and plastic deformation to facilitate NR invagination as a mechanical feedback mechanism<sup>14</sup>. This finding suggests that the elastoplastic transition is a key mechanism in certain aspects of embryogenesis. In



contrast, other studies have reported that NR invagination is also driven by cell migration and basal constriction in fish, frogs, and birds<sup>62–64</sup>. Therefore, further investigation is required to explore the specific contexts and mechanisms by which the elastoplastic transition of the epithelium is utilized in embryogenesis.

In conclusion, we demonstrated that cells actively control the irreversibility of epithelial folding through an elastoplastic transition. This observation requires the reconsideration of long-standing mechanistic concepts in development, indicating that epithelial morphogenesis proceeds not only by regulating active force generation

**Fig. 4 | Actin bracket formation establishes elastoplastic transition with a tunable critical duration.** **a** Time-lapse images of Lifeact-mCherry before indentation and at  $t = 0$  min,  $t = 10$  min, and  $t = 30$  min. F-actin accumulated at fold (arrows). Seven experiments were repeated independently. Scale bars,  $15\ \mu\text{m}$ . **b** Three-dimensional constructed images of SPY650-actin at  $t = 0$  min and  $t = 30$  min. Dotted lines indicate epithelial contours. F-actin accumulated around apical and lateral boundaries (arrows). Kymographs of Lifeact-mCherry intensity along the epithelium contour (**c**) and apicobasal axis (**d**) over time. Intensity at each pixel was normalized to the initial intensity and averaged across samples ( $N = 3$ ). **e** Time variation of the maximum and average Lifeact-mCherry intensity around fold. **f** Bending plastic ratio,  $\psi$ , under drug treatment for F-actin dynamics inhibition. For  $\tau = 5$  min, the condition included treatment with cytochalasin D ( $p = 0.0683$ ) and Jasplakinolide ( $p = 1.95 \times 10^{-4}$ ). For  $\tau = 30$  min, the condition included treatment with cytochalasin D ( $p = 1.77 \times 10^{-4}$ ), Latrunculin A ( $p = 8.94 \times 10^{-7}$ ), CK-666 ( $p = 0.0225$ ), and Jasplakinolide ( $p = 0.894$ ). **g** Lifeact-mCherry intensity around the apex under drug treatment conditions targeting F-actin polymerization inhibition, EGFR inhibition, and mechanosensitive channel inhibition, as well as under a condition of low-curvature folding. For  $\tau = 5$  min, the conditions included indentation only ( $p = 0.00524$ ), treatment with cytochalasin D ( $p = 0.387$ ) and Jasplakinolide ( $p = 0.00264$ ). For  $\tau = 30$  min, the conditions included indentation only

( $p = 5.42 \times 10^{-5}$ ), treatment with cytochalasin D ( $p = 0.364$ ), Latrunculin A ( $p = 0.223$ ), CK666 ( $p = 0.105$ ), Jasplakinolide ( $p = 0.00334$ ), PD153035 ( $p = 0.343$ ), LY294002 ( $p = 0.485$ ), Ipatasertib ( $p = 0.451$ ), PD0325901 ( $p = 0.00110$ ), GsMTx4 ( $p = 0.203$ ), BAPTA-AM ( $p = 0.0631$ ), Pico145 ( $p = 0.00866$ ), Pyr3 ( $p = 0.301$ ), SAR7334 ( $p = 0.925$ ), and low-curvature folding ( $p = 0.0190$ ). Values were normalized to those before indentation. **h** Bending plastic ratio,  $\psi$ , as a function of duration time,  $\tau$ , under conditions of actin polymerization inhibition or enhancement. Dotted lines show fitted sigmoid functions. **i** Mechanical indentation device combined with a local pharmacological intervention. Two glass pipettes were used for indentation and release of inhibitors, respectively. **j** Time-lapse images of Lifeact-mCherry during hold, at  $t = 30$  min, and 5 min after pipette retraction. **k** Bending plastic ratio,  $\psi$ , under conditions of local cytochalasin D release at the fold ( $p = 0.00944$ ) and at the region away from the fold ( $p = 0.113$ ) for  $\tau = 30$  min. **l** Lifeact-mCherry intensity around the apex for  $\tau = 30$  min, under conditions of local cytochalasin D release at the fold ( $p = 9.90 \times 10^{-4}$ ) and the region away from the fold ( $p = 0.171$ ). Box plots in (**f**, **g**, **k**, **l**): center, median; bounds, 25th and 75th percentiles; whiskers, min and max; \* $P < 0.05$ , \*\* $P < 0.01$ , \*\*\* $P < 0.001$  (two-sided Welch's  $t$ -test).  $N$  indicates a biologically independent sample. EGFR epidermal growth factor receptor. Source data are provided as a Source Data file.

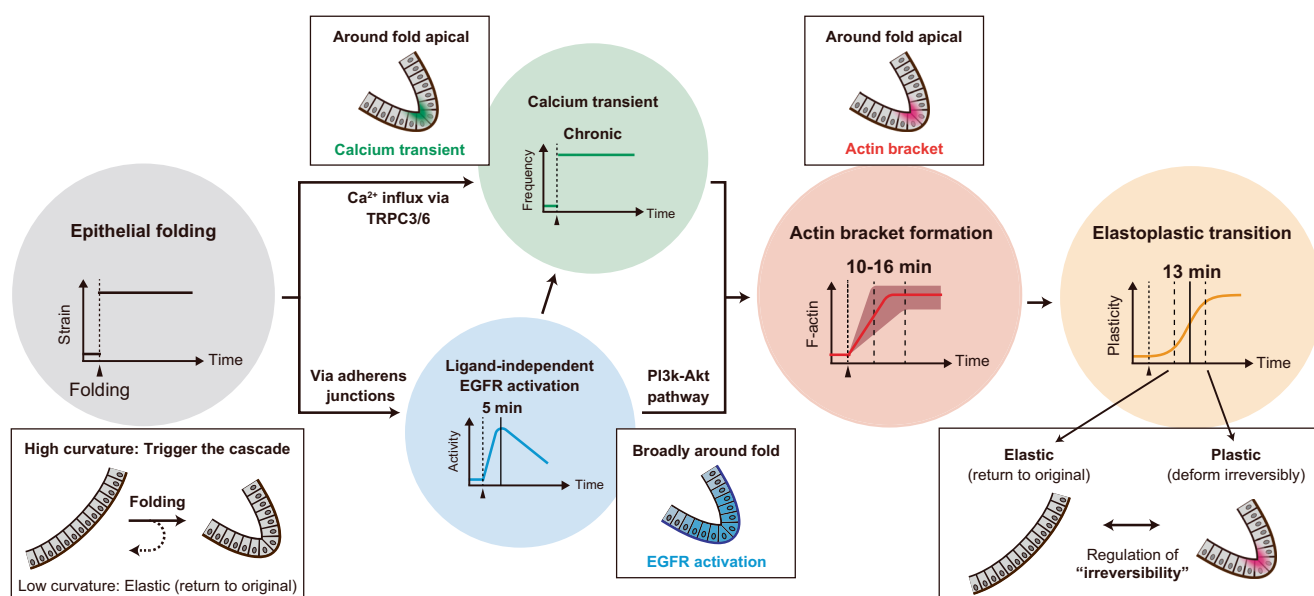


**Fig. 5 | Summary of elastoplastic transition in epithelial folding via mechanosensitive actin bracket formation.** A large bending deformation applied to the epithelial sheet activates two mechanosensitive pathways: ligand-independent epidermal growth factor receptor (EGFR) activation and transient receptor potential canonical (TRPC) 3/6-mediated calcium influx, each independently triggered by deformation. EGFR activation occurs around the fold, peaking at 5 min and then gradually decreasing. This EGFR activation requires adherens junctions.

Under this EGFR activation, calcium influx is specifically triggered at the apical side of the fold and persists for the duration of the deformation. These signals induce actin accumulation at the fold. The region of actin accumulation expands for  $-13 \pm 3$  min, forming a bracket structure. This mechanosensitive actin bracket formation drives the elastoplastic transition, switching the epithelial response from elastic to plastic, thereby determining the irreversibility of epithelial folding.

but also by regulating deformation irreversibility to define the resulting morphology.

## Methods

### Mice

All mouse studies were performed with approval from the Ethics Committee at Kanazawa University. We used Slc:ICR mice purchased from Sankyo Labo Service Co. (Toyama, Japan). We defined the mid-night preceding the detection of a plug as embryonic day 0.0 (E0.0), and all mice were euthanized by cervical dislocation.

### Cell culture

Madin-Darby canine kidney (MDCK) cells were obtained from the Mostov Lab at the University of California, San Francisco. Cell lines stably expressing Lifeact-mCherry and GCaMP6s stable

were established. MDCK-WT-EKARrEV, MDCK-4KO-EKARrEV, MDCK-dADAM17-EKARrEV, MDCK-dEGF-EKARrEV, and MDCK- $\alpha$ catenin KO-EKARrEV cells expressing a FRET biosensor for ERK activity were contributed by Dr. Michiyuki Matsuda (Kyoto University, Kyoto)<sup>34</sup>. These cells were maintained in Dulbecco's Modified Eagle Medium (DMEM, Wako, Catalog#: 043-30085) containing 10% Fetal Bovine Serum (FBS, Gibco, Catalog#: 26140079 or NICHIREI, Catalog#: 175012) and 1% penicillin-streptomycin (Wako, Catalog#: 168-23191) in a 5% CO<sub>2</sub> incubator at 37 °C.

Mouse embryonic stem cells (mESCs, EB5, Rx-GFP) were maintained as described in previous studies<sup>65,66</sup>, as detailed below. The cells were maintained in Glasgow's Minimum Essential Medium (GMEM, Nacalai, Catalog#: 12965-65) containing 10% Knockout Serum Replacement (KSR, Gibco, Catalog#: 10828-028), 1% FBS (NICHIREI, Catalog#: 175012), 1% Non-essential Amino Acids (NEAA, Wako, Catalog#:



139-15651), 1 mM Pyruvate (Wako, Catalog#: 190-14881), 0.1 mM 2-Mercaptoethanol (2-ME, Sigma-Aldrich, Catalog#: M6250), 20  $\mu$ l of  $10^6$  units/ml LIF (Sigma-Aldrich, Catalog#: ESG1107), and 20  $\mu$ l of 10 mg/ml blasticidin (Cayman, Catalog#: 14499) in a gelatin-coated 10 cm dish. We used a subline of the mESC line EB5 (129/Ola), in which the GFP gene was knocked in under the Rx promoter (RIKEN BioResource Research Center, ID: AES0145).

### Establishment of stable cell lines

To establish MDCK cells that stably express Lifeact-mCherry, a lentiviral transduction system was used. The lentivirus was produced by co-transfection of the expression vector coding Lifeact-mCherry and lentiviral packaging plasmids (pCMVdr8.91 and pMD2.G) using PEI MAX (Polysciences, Catalog#: 24765) into HEK293T cells. The viral supernatant was collected 48 h after the co-transfection and filtered through a 0.45  $\mu$ m filter. Then MDCK cells were infected with the viral supernatant in the presence of hexadimethrine bromide (Sigma-Aldrich, Catalog#: H9268). After a few days, fluorescent cells were sorted using a cell sorter (FACSMelody™, BD Bioscience).

To establish MDCK cells that stably express GCaMP6s, a PiggyBac transposase system was used. The expression vector coding GCaMP6s was introduced into MDCK cells with Super PiggyBac transposase (System Bioscience, Catalog#: PB510-1). After a few days, fluorescent cells were sorted using a cell sorter (SH800, SONY).

### Plasmids

Lifeact-mCherry<sup>67</sup> was obtained from Michael Davidson (Addgene, Catalog#: 54491). The coding sequence of Lifeact-mCherry was amplified with the primers 5'-AATTCTCACGCGGCCGCCACCATGG GCGTGGCCGACTTG-3' and 5'-TCAAGCTTGCATGCCTGCAGTTACTT GTACAGCTCGTCCATGCCGC-3', and cloned via In-Fusion HD cloning (Clontech, Catalog#: Z9648N) into a modified pHR'SIN:CSW vector under an EF1 $\alpha$  promoter.

The GCaMP6s coding sequence amplified from pGP-CMV-GCaMP6s<sup>67</sup> purchased from Addgene (Catalog#: 40753) with the primers 5'-GGGGAATTCGCCACCATGGGTTCTCA-3' and 5'-CCCGCGGC CGCTCACTTCGCTGTCATCA-3' was subcloned into EcoRI (Takara, Catalog#: 1040 A) and NotI (Thermo Scientific, Catalog#: FD0594) sites in the PB-CMV-MCS-EF1 $\alpha$ -Puro PiggyBac transposon vector (System Bioscience, Catalog#: PB510B-1).

### Three-dimensional culture for MDCK cell-derived cyst generation

Epithelial cysts were derived from MDCK cells according to the previously reported method<sup>68,69</sup>, as detailed below. A total of 50  $\mu$ l Matrigel (Corning, Catalog#: 354230) was polymerized on a 15-mm diameter cover glass (MATSUNAMI, Catalog#: C015001) at the bottom of a 24-well plate. Cell suspension containing 2% Matrigel was poured into the culture medium to obtain a final cell density of 10,000 cells/cm<sup>2</sup>. After ~7 days of culture, spherical epithelial cysts with a lumen were obtained in the gel on the cover glass.

### SFEBq for optic vesicle organoid generation

The SFEBq culture method was performed as described in a previous study<sup>65</sup>, as detailed below. In total, 3000 cells were suspended in 100  $\mu$ l of differentiation medium in each well of 96-well plate, marking day 0. On day 1, Matrigel (Corning, Catalog#: 354230) were added to each well to reach a final concentration of 2.0%. The differentiation medium was GMEM containing 1.5% KSR, 1% NEAA, 1 mM Pyruvate, and 0.1 mM 2-ME. Tissues from days 6 or 7, with protruding Rx-positive regions, were used for the indentation assay.

### Mouse embryonic OV culture

The culture of mouse embryonic optic vesicles was performed as described in a previous study<sup>14</sup>, as detailed below. Mice were dissected

at E9.0, and the heads were cut off and cultured in DMEM Ham's/F12 (Wako, Catalog#: 048-29785) supplemented with 1% N-2 supplement (Gibco, Catalog#: 17502-048) and 1% penicillin-streptomycin (Wako, Catalog#: 168-23191) in a 5% CO<sub>2</sub> incubator at 37 °C. For the mechanical indentation assay, heads were used within 6 h of the start of incubation.

### Mechanical indentation assay

To perform the mechanical indentation assay under well-controlled conditions, we developed a custom incubator placed on the stage of a confocal microscope (LSM800, Zeiss). This incubator was maintained at conditions of 5% CO<sub>2</sub>, 37 °C, and  $\geq 90\%$  humidity. In addition, we installed a three-axis piezoelectric manipulator (MM3A-LA, Kleindiek Nanotechnik) equipped with a pipette inside the incubator. To avoid adhesion of the pipette to tissues, the tip surface was coated with methacryloyloxyethyl phosphorylcholine polymers (NovyCoat, FastGene, Catalog#: FG-NVC100).

For indentation assays using mouse embryonic OV tissue and mESC-derived OV organoids, samples were transferred to 35-mm diameter glass-bottom dishes and embedded in Matrigel with 1 ml of culture medium. For indentation assays using MDCK cell-derived cysts, single-layer, single-lumen cysts with an average diameter ( $55 \pm 6$   $\mu$ m) were selected from among 7–10-day-old cysts. The cysts were cultured in Matrigel on a coverslip, which was transferred to a 35-mm-diameter dish filled with 1 ml culture medium. Using the manipulator, a pipette was used to indent the epithelium to induce a fold at  $t = 0$ , held for the duration of  $\tau$ , and retracted at  $t = \tau$ . The epithelium was indented to induce a fold with a high amount of curvature, with the outer curvature  $\kappa > 0.125$   $\mu$ m<sup>-1</sup>. However, when examining the effect of the curvature of folding, the epithelium was indented to induce a lower amount of curvature, with  $\kappa < 0.10$   $\mu$ m<sup>-1</sup>. After retraction, the epithelium reached a stable shape within 5 min. Therefore, the epithelium shape was evaluated at  $t = \tau + 5$  min. For  $\tau = 30$  min, the stable shape was maintained for 2–3 h after retraction. Thereafter, the shape of the epithelium gradually changed due to cell migration.

For FRET and calcium imaging, cysts were resuspended in a collagen gel to eliminate growth factors and facilitate the detection of sensitive signals. Cysts were incubated with cell recovery solution (Corning, Catalog#: 354253) on ice for 20 min to depolymerize Matrigel and then collected by centrifugation at  $300 \times g$  for 3 min. Cysts were suspended in 50  $\mu$ l collagen solution consisting of 70% collagen (0.3% CellMatrix Type I-A, Nitta Gelatin, Catalog#: 637-00653), 20% Hank's Balanced Salt Solution (HBSS, without phenol red, Wako, Catalog#: 082-08961), and 10% reconstitution buffer (Nitta Gelatin, Catalog#: 635-00791). Cysts in collagen solution were placed in a 35-mm-diameter glass-bottom dish, and collagen was allowed to polymerize at 37 °C for 20 min. The dish was filled with 1 ml culture medium.

### Quantification of curvature and intensity

The curvature and fluorescence intensity along the epithelium contour were calculated using three-point method as described in previous studies<sup>70,71</sup>, as detailed below. For preprocessing, a mask image of the epithelium contour was manually obtained from the transmitted light image of the tissue. The local curvature was calculated as the inverse of radius of fitting circle. The circle passes three points; one is the sampling point where the curvature is measured, others are at a distance of  $\pm 8.3$   $\mu$ m along the contour from the sampling point. Fluorescence intensity was calculated as the average in the direction normal to the contour from each sampling point.

### Quantification of entire cyst and lumen volumes

The entire cyst and lumen volumes were calculated from the cross-sectional images during indentation. Masks of the entire cyst and the lumen regions were manually created from the images. Assuming that the cyst shape is rotationally symmetric in three dimensions, the

volumes were calculated by rotating the masks around the center axis. The center axis was determined based on the location and direction of the pipette used for indentation.

### Quantification of epithelial bending plastic ratio

To quantify the mechanical response of the epithelium, we introduced a parameter,  $\psi$ , to represent the degree of bending plastic ratio. This parameter is determined using the maximum curvature on the epithelium contour, specifically at a location we refer to as the apex. We measured curvature at the apex at  $t = \tau$  and  $t = \tau + 5$  min. We refer to the curvature at  $t = \tau$  as the curvature of the applied fold,  $\kappa$ , whereas the curvature at  $t = \tau + 5$  min is the curvature of the relaxed shape,  $\kappa_1$ . In addition, we identified the pre-indentation location on the epithelium that corresponds to the apex immediately after the indentation begins ( $t = 0$ ). We measured the average curvature around this location, represented by  $\kappa_0$ . The degree of bending plastic ratio,  $\psi$ , is defined as

$$\psi = \frac{\kappa_1 - \kappa_0}{\kappa - \kappa_0}.$$

The value for bending plastic ratio ranges from 0 to 1. When  $\psi = 0$ , the epithelium responds completely elastically, retaining its original shape after pipette removal. Conversely, when  $\psi = 1$ , the epithelium responds completely plastically, maintaining the applied fold.

### Sigmoid curve fitting to bending plastic ratio

We employed sigmoidal functions to evaluate the dependence of bending plastic ratio on  $\tau$  and  $\kappa$ . The functions fitted to the dependences on  $\tau$  and  $\kappa$ , represented by  $\psi_\tau$  and  $\psi_\kappa$ , are described by

$$\psi_\tau(\tau) = \frac{\psi_\tau^\infty}{1 + \exp \alpha_\tau(\tau_{ct} - \tau)}$$

and

$$\psi_\kappa(\kappa) = \frac{\psi_\kappa^\infty}{1 + \exp \alpha_\kappa(\kappa_{ct} - \kappa)}$$

respectively. Here,  $\psi_\tau^\infty$ ,  $\alpha_\tau$ ,  $\tau_{ct}$ ,  $\psi_\kappa^\infty$ ,  $\alpha_\kappa$ , and  $\kappa_{ct}$  are constants, and  $\tau_{ct}$  and  $\kappa_{ct}$  represent the critical duration and curvature, respectively. By fitting these equations to the data using the least squares method, we determined the values of  $\tau_{ct}$  and  $\kappa_{ct}$ .

### Mechanical measurement of Matrigel

The mechanical properties of Matrigel were quantified using atomic force microscopy (AFM). A 50  $\mu$ l drop of 100% Matrigel was polymerized into a dome-like shape on a dish. AFM measurements were conducted using a cantilever (NANOSENSORS, TL-CONT) with a 94  $\mu$ m diameter polystyrene bead (Asone), similar in size to the glass pipette tip used in the indentation assay. The cantilever was pressed at a rate of 1.88  $\mu$ m/s to a depth of  $12.7 \pm 1.2$   $\mu$ m (mean  $\pm$  s.d.), reflecting the indentation depth of the pipette during the indentation assay. A force of 10 nN was applied by the cantilever. To mimic the conditions of the indentation assay, the polymerized Matrigel was incubated in culture medium for 1 week. Young's modulus was determined by analyzing the resulting force curves using the Hertzian model (spherical) fitted with JPKSPM Data Processing software (Bruker). While Young's modulus of Matrigel was  $36.0 \pm 2.3$  Pa immediately after polymerization, it decreased to  $12.1 \pm 2.2$  Pa after 1 week of incubation. The relaxation time of Matrigel was assessed by measuring stress relaxation during a 30-s force application. The relaxation time was calculated by fitting the following exponential function of stress variation over time,

represented by  $S$ :

$$S(t) = S_0 \exp\left(-\frac{t}{\tau}\right) + S_\infty.$$

Here,  $S_0$ ,  $S_\infty$ , and  $\tau$  are constants, with  $S_\infty$  and  $\tau$  representing the stress when reaching steady state and the relaxation time, respectively. We obtained the values of  $S_\infty$  and  $\tau$  using the least squares method.

### Three-dimensional imaging of F-actin

Three-dimensional imaging was performed to observe changes in the three-dimensional structure of accumulated F-actin at the fold during the indentation. Cysts were incubated in a culture medium containing SPY650-FastAct (1:2000 dilution, Cytoskeleton, Inc., Catalog#: CY-SC505) for 3 h before indentation. Fluorescence observations were made by confocal microscopy immediately after pipette indentation and during holding.

### Pharmaceutical interventions

To examine molecular activities, cysts were treated with the actin polymerization inhibitors cytochalasin D (Abcam, Catalog#: ab143484; 10  $\mu$ M, 60-min incubation) or latrunculin A (Wako, Catalog#: 125-04363; 10  $\mu$ M, 60-min incubation); the ARP2/3 complex inhibitor CK666 (Merck, Catalog#: SML0006; 100  $\mu$ M, 60-min incubation); the actin polymerization inducer and actin depolymerization inhibitor jasplakinolide (Abcam, Catalog#: ab141409; 1  $\mu$ M, 60-min incubation); the EGFR inhibitor PD153035 (TCI, Catalog#: B4945; 1  $\mu$ M, overnight [O/N] incubation); the MEK inhibitor PD0325901 (MedChemExpress, Catalog#: HY-10254; 10  $\mu$ M, 60-min incubation); the PI3K inhibitor LY294002 (MedChemExpress, Catalog#: HY-10108; 50  $\mu$ M, O/N incubation); the Akt inhibitor ipatasertib (MedChemExpress, Catalog#: HY-15186; 1  $\mu$ M, O/N incubation); the mechanosensitive cation channel inhibitor (e.g., Piezo1, TRPC1/6) GsMTx4 (Abcam, Catalog#: ab141871 or Peptide Institute, Catalog#: 4393-s; 2.5  $\mu$ M, 15-min incubation); the intracellular calcium chelator BAPTA-AM (Tronto Research Chemicals, Catalog#: B123700; 25  $\mu$ M, 60-min incubation); the TRPC1 inhibitor Pico145 (Adooq Bioscience, Catalog#: A13344; 1 nM, 15-min incubation); the TRPC3 inhibitor Pyr3 (Merck, Catalog#: 648490; 3  $\mu$ M, 15-min incubation); or the TRPC6 inhibitor SAR-7334 (Selleck, Catalog#: S6634; 100 nM, 15-min incubation). EGFR downstream signaling molecules (MEK, PI3K, and Akt) were pharmacologically inhibited using inhibitors with specific activity for each target molecule<sup>31,72</sup>. These inhibitors, widely utilized in previous studies, effectively suppress the functions of their target molecules while minimizing side effects<sup>72–74</sup>.

### Confocal FRET imaging

FRET images were obtained and processed using the method described in our previous study<sup>75</sup>, as detailed below. To eliminate growth factors from the gel and enable the detection of sensitive signals, cysts were resuspended in a collagen gel before performing FRET imaging, and media was replaced with HBSS supplemented with calcium and magnesium and without phenol red at least 1 h before the indentation assay to eliminate growth factors from the media. Time-lapse images were acquired using a confocal microscope (FV-3000, Olympus) equipped with a 20 $\times$  Objective lens (20 $\times$ -UPlanXApo, Olympus), a GaAsP detector (FV31-HSD, Evident), and a dichroic mirror (U-FBNA, Olympus). A 405 nm laser was used to excite cyan fluorescent protein (CFP). Emission was detected at 460–480 nm for CFP (donor) and 510–530 nm for yellow fluorescent protein (YFP, acceptor). The FRET/CFP ratio was calculated after subtracting the background, and only regions with high YFP signal were visualized using ImageJ.

### Calcium transient measurement

To observe calcium transients, cysts stably expressing GCaMP6s were resuspended in collagen gel. Time-lapse images were acquired for 1 min at each of three time points: before, 10 min after, and 20 min after indentation. To detect fast calcium responses, acquisition conditions were set to  $128 \times 128$  pixels, with a frame interval of ~130 ms.

To quantify the calcium transient frequency, GCaMP6s images were processed using ImageJ. Prior to processing, each image was smoothed by calculating the median value over each frame and time period at each pixel. The base fluorescence intensity level at each pixel was subtracted from the images and calculated as a moving average in the time direction over a width of 50 frames before and 50 frames after the central image. The number of calcium transients was calculated as the number of times that the difference between adjacent time frames at each pixel exceeded a value 15% higher than the average of all time frame images.

The distribution of calcium transient frequency along the epithelial contour over time was determined by normalizing the value of each pixel against the ratio of the average of each experiment to the average of all experiments, averaging the frequency in 5 pixels from the apical side in each experiment, and calculating statistical values between multiple experiments. Statistical values comparing indentation alone with indentation in the presence of pharmaceutical inhibitors and comparing the apical and basal sides were calculated by normalizing the value of each pixel against the ratio of the average before to the average after indentation for each experiment. The data after indentation include measurements conducted at 10 and 20 min after indentation. The length and thickness of the region in which a high frequency of calcium transients was detected were estimated by fitting Gaussian functions to the frequency distributions along the contour and apicobasal axes, respectively, centered on the maximum value in the average map.

### Statistical analysis of F-actin distribution

To quantify the spatial distribution of F-actin, Lifeact-mCherry images were processed using ImageJ. Each image was smoothed by calculating the median value over each frame and time period at each pixel. The epithelial contour was manually determined, and each fluorescence image was transformed into a map along the contour and apicobasal axes. The resulting maps were averaged across experiments by aligning each apex with the highest curvature along the contour axis and each apical surface along the apicobasal axis. The average value around the apex was calculated from the average map by defining regions of  $5 \times 1$ ,  $10 \times 2$ ,  $20 \times 4$ , and  $40 \times 8$  pixels. The regions were set around the pixel with the highest intensity at the apex. The length and thickness of each actin bracket were estimated by fitting Gaussian functions to the intensity distributions along the contour and apicobasal axes, respectively, centered on the maximum value in the average map.

To conduct simultaneous observations of F-actin and calcium transients, cysts derived from GCaMP6s-expressing cells were stained with SPY650-FastAct. Lifeact-mCherry intensity values and calcium transient frequencies were obtained at each position along the epithelial contour.

### Local application of actin polymerization inhibitor

To locally inhibit actin polymerization in a cyst, the actin polymerization inhibitor cytochalasin D was applied using a sharp glass pipette. A 10 mM solution of cytochalasin D, mixed with 0.5 mg/ml FITC-conjugated dextran (TdB Labs, Catalog#: FD4), was applied by pressure ejection using a FemtoJet 4x (Eppendorf). The ejection was pulsed to create a local concentration gradient of the inhibitor.

### Statistics and reproducibility

The statistical tests were performed using Microsoft Excel to obtain the  $p$  values. Asterisks indicate statistical significance ( $*p < 0.05$ ,  $**p < 0.01$ , and  $***p < 0.001$ ). No statistical method was used to pre-determine sample size. To ensure the quality of the experimental data, we excluded data if the sample collapsed or moved outside of the field during the mechanical indentation assay. The experiments were not randomized. The investigators were not blinded to allocation during experiments and outcome assessment.

### Reporting summary

Further information on research design is available in the Nature Portfolio Reporting Summary linked to this article.

### Data availability

All the data used to generate figures in this paper are provided in the Supplementary Information and Source Data file. The full image dataset is available on request to the corresponding author. Source data are provided with this paper.

### References

- Martin, A. C. & Goldstein, B. Apical constriction: themes and variations on a cellular mechanism driving morphogenesis. *Development* **141**, 1987–1998 (2014).
- Sawyer, J. M. et al. Apical constriction: a cell shape change that can drive morphogenesis. *Dev. Biol.* **341**, 5–19 (2010).
- Martin, A. C., Kaschube, M. & Wieschaus, E. F. Pulsed contractions of an actin–myosin network drive apical constriction. *Nature* **457**, 495–499 (2009).
- Kondo, T. & Hayashi, S. Mitotic cell rounding accelerates epithelial invagination. *Nature* **494**, 125–129 (2013).
- Takeichi, M. Dynamic contacts: rearranging adherens junctions to drive epithelial remodelling. *Nat. Rev. Mol. Cell Biol.* **15**, 397–410 (2014).
- von Dassow, M. & Davidson, L. A. Variation and robustness of the mechanics of gastrulation: the role of tissue mechanical properties during morphogenesis. *Birth Defects Res. C Embryo Today* **81**, 253–269 (2007).
- Davidson, L. A. et al. Emergent morphogenesis: elastic mechanics of a self-deforming tissue. *J. Biomech.* **43**, 63–70 (2010).
- Khalilgharibi, N. et al. Stress relaxation in epithelial monolayers is controlled by the actomyosin cortex. *Nat. Phys.* **15**, 839–847 (2019).
- Mongera, A. et al. Mechanics of the cellular microenvironment as probed by cells in vivo during zebrafish presomitic mesoderm differentiation. *Nat. Mater.* **22**, 135–143 (2023).
- He, B., Doubrovinski, K., Polyakov, O. & Wieschaus, E. Apical constriction drives tissue-scale hydrodynamic flow to mediate cell elongation. *Nature* **508**, 392–396 (2014).
- Mao, Y. & Baum, B. Tug of war—the influence of opposing physical forces on epithelial cell morphology. *Dev. Biol.* **401**, 92–102 (2015).
- Davidson, L. A. Epithelial machines that shape the embryo. *Trends Cell Biol.* **22**, 82–87 (2012).
- Matamoro-Vidal, A. & Levayer, R. Multiple influences of mechanical forces on cell competition. *Curr. Biol.* **29**, R762–R774 (2019).
- Okuda, S. et al. Strain-triggered mechanical feedback in self-organizing optic-cup morphogenesis. *Sci. Adv.* **4**, eaau1354 (2018).
- Petridou, N. I., Corominas-Murtra, B., Heisenberg, C. P. & Hannezo, E. Rigidity percolation uncovers a structural basis for embryonic tissue phase transitions. *Cell* **184**, 1914–1928 (2021).
- Tetley, R. J. et al. Tissue fluidity promotes epithelial wound healing. *Nat. Phys.* **15**, 1195–1203 (2019).
- Petridou, N. I., Grigolon, S., Salbreux, G., Hannezo, E. & Heisenberg, C.-P. Fluidization-mediated tissue spreading by mitotic cell rounding and non-canonical Wnt signalling. *Nat. Cell Biol.* **21**, 169–178 (2019).



18. Wyatt, T. P. J. et al. Actomyosin controls planarity and folding of epithelia in response to compression. *Nat. Mater.* **19**, 109–117 (2020).
19. Luciano, M., Versaevel, M., Kalukula, Y. & Gabriele, S. Mechanoreponse of curved epithelial monolayers lining bowl-shaped 3D microwells. *Adv. Healthc. Mater.* <https://doi.org/10.1002/adhm.202203377> (2023).
20. Davidson, L. A. Embryo mechanics: balancing force production with elastic resistance during morphogenesis. *Curr. Top. Dev. Biol.* **95**, 215–241 (2011).
21. Harris, A. R. et al. Characterizing the mechanics of cultured cell monolayers. *Proc. Natl. Acad. Sci. USA* **109**, 16449–16454 (2012).
22. Latorre, E. et al. Active superelasticity in three-dimensional epithelia of controlled shape. *Nature* **563**, 203–208 (2018).
23. Discher, D. E., Janmey, P. & Wang, Y. Tissue cells feel and respond to the stiffness of their substrate. *Science* **310**, 1139–1143 (2005).
24. Vogel, V. & Sheetz, M. Local force and geometry sensing regulate cell functions. *Nat. Rev. Mol. Cell Biol.* **7**, 265–275 (2006).
25. Mao, Y. et al. Differential proliferation rates generate patterns of mechanical tension that orient tissue growth. *EMBO J.* **32**, 2790–2803 (2013).
26. Coste, B. et al. Piezo proteins are pore-forming subunits of mechanically activated channels. *Nature* **483**, 176–181 (2012).
27. Baptista, D., Teixeira, L., van Blitterswijk, C., Giselbrecht, S. & Truckenmüller, R. Overlooked? Underestimated? Effects of substrate curvature on cell behavior. *Trends Biotechnol.* **37**, 838–854 (2019).
28. Luciano, M. et al. Cell monolayers sense curvature by exploiting active mechanics and nuclear mechanoadaptation. *Nat. Phys.* **17**, 1382–1390 (2021).
29. Tang, W. et al. Collective curvature sensing and fluidity in three-dimensional multicellular systems. *Nat. Phys.* **18**, 1371–1378 (2022).
30. Sun, F., Fang, C., Shao, X., Gao, H. & Lin, Y. A mechanism-based theory of cellular and tissue plasticity. *Proc. Natl. Acad. Sci. USA* **120**, e2305375120 (2023).
31. Reichel, S. & Kaliske, M. Hygro-mechanically coupled modelling of creep in wooden structures, Part I: mechanics. *Int. J. Solids Struct.* **77**, 28–44 (2015).
32. Tschumperlin, D. J. et al. Mechanotransduction through growth-factor shedding into the extracellular space. *Nature* **429**, 83–86 (2004).
33. Sullivan, B. et al. Mechanical disruption of E-cadherin complexes with epidermal growth factor receptor activates growth factor-dependent signaling. *Proc. Natl. Acad. Sci. USA* **119**, e2100679119 (2022).
34. Lin, S. et al. Redundant roles of EGFR ligands in the ERK activation waves during collective cell migration. *Life Sci. Alliance* **5**, e202101206 (2022).
35. Cavallaro, U. & Christofori, G. Cell adhesion and signalling by cadherins and Ig-CAMs in cancer. *Nat. Rev. Cancer* **4**, 118–132 (2004).
36. Perez, T. D., Tamada, M., Sheetz, M. P. & Nelson, W. J. Immediate-early signaling induced by E-cadherin engagement and adhesion. *J. Biol. Chem.* **283**, 5014–5022 (2008).
37. Guo, G. et al. Ligand-independent EGFR signaling. *Cancer Res.* **75**, 3436–3441 (2015).
38. Lambert, S., Vind-Kezunovic, D., Karvinen, S. & Gniadecki, R. Ligand-independent activation of the EGFR by lipid raft disruption. *J. Invest. Dermatol.* **126**, 954–962 (2006).
39. Moro, L. et al. Integrin-induced epidermal growth factor (EGF) receptor activation requires c-Src and p130Cas and leads to phosphorylation of specific EGF receptor tyrosines. *J. Biol. Chem.* **277**, 9405–9414 (2002).
40. Rao, T. C. et al. EGFR activation attenuates the mechanical threshold for integrin tension and focal adhesion formation. *J. Cell Sci.* **133**, jcs238840 (2020).
41. Saxena, M. et al. EGFR and HER2 activate rigidity sensing only on rigid matrices. *Nat. Mater.* **16**, 775–781 (2017).
42. Umesh, V., Rape, A. D., Ulrich, T. A. & Kumar, S. Microenvironmental stiffness enhances glioma cell proliferation by stimulating epidermal growth factor receptor signaling. *PLoS ONE* **9**, e101771 (2014).
43. Muhamed, I. et al. E-cadherin-mediated force transduction signals regulate global cell mechanics. *J. Cell Sci.* **129**, 1843–1854 (2016).
44. Bae, C., Sachs, F. & Gottlieb, P. A. The mechanosensitive ion channel Piezo1 is inhibited by the peptide GsMTx4. *Biochemistry* **50**, 6295–6300 (2011).
45. Gailly, P. TRP channels in normal and dystrophic skeletal muscle. *Curr. Opin. Pharmacol.* **12**, 326–334 (2012).
46. Bandyopadhyay, B. C. et al. Apical localization of a functional TRPC3/TRPC6-Ca<sup>2+</sup>-signaling complex in polarized epithelial cells: role in apical Ca<sup>2+</sup> influx. *J. Biol. Chem.* **280**, 12908–12916 (2005).
47. Liang, C. et al. Towards an integrative understanding of cancer mechanobiology: calcium, YAP, and microRNA under biophysical forces. *Soft Matter* **18**, 1112–1148 (2022).
48. Sanderson, M. J., Charles, A. C. & Dirksen, E. R. Mechanical stimulation and intercellular communication increases intracellular Ca<sup>2+</sup> in epithelial cells. *Cell Regul.* **1**, 585–596 (1990).
49. Liu, J. et al. PI3K/Akt-dependent phosphorylation of GSK3 $\beta$  and activation of RhoA regulate Wnt5a-induced gastric cancer cell migration. *Cell. Signal.* **25**, 447–456 (2013).
50. Deng, S. et al. PI3K/AKT signaling tips the balance of cytoskeletal forces for cancer progression. *Cancers* **14**, 1652 (2022).
51. Qian, Y. et al. PI3K induced actin filament remodeling through Akt and p70S6K1: implication of essential role in cell migration. *Am. J. Physiol. Cell Physiol.* **286**, C153–C163 (2004).
52. Courtney, T. H. *Mechanical Behavior of Materials* 2nd edn, 630–685 (McGraw-Hill International Editions, Singapore, 2000).
53. Krajnc, M., Dasgupta, S., Zihler, P. & Prost, J. Fluidization of epithelial sheets by active cell rearrangements. *Phys. Rev. E* **98**, 22409 (2018).
54. Ranft, J. et al. Fluidization of tissues by cell division and apoptosis. *Proc. Natl. Acad. Sci. USA* **107**, 20863–20868 (2010).
55. Lardennois, A. et al. An actin-based viscoplastic lock ensures progressive body-axis elongation. *Nature* **573**, 266–270 (2019).
56. Lecuit, T. & Lenne, P.-F. Cell surface mechanics and the control of cell shape, tissue patterns and morphogenesis. *Nat. Rev. Mol. Cell Biol.* **8**, 633–644 (2007).
57. Suzuki, M. et al. Distinct intracellular Ca<sup>2+</sup> dynamics regulate apical constriction and differentially contribute to neural tube closure. *Development* **144**, 1307–1316 (2017).
58. Ogura, Y., Wen, F.-L., Sami, M. M., Shibata, T. & Hayashi, S. A switch-like activation relay of EGFR-ERK signaling regulates a wave of cellular contractility for epithelial invagination. *Dev. Cell* **46**, 162–172 (2018).
59. Hirashima, T. & Matsuda, M. ERK-mediated curvature feedback regulates branching morphogenesis in lung epithelial tissue. *Curr. Biol.* **34**, 683–696 (2024).
60. Brodu, V. & Casanova, J. The RhoGAP crossveinless-c links trachealess and EGFR signaling to cell shape remodeling in *Drosophila* tracheal invagination. *Genes Dev.* **20**, 1817–1828 (2006).
61. Levayer, R. & Lecuit, T. Oscillation and polarity of E-cadherin asymmetries control actomyosin flow patterns during morphogenesis. *Dev. Cell* **26**, 162–175 (2013).
62. Cardozo, M. J., Sánchez-Bustamante, E. & Bovolenta, P. Optic cup morphogenesis across species and related inborn human eye defects. *Development* **150**, dev200399 (2023).



63. Kwan, K. M. et al. A complex choreography of cell movements shapes the vertebrate eye. *Development* **139**, 359–372 (2012).
64. Holt, C. Cell movements in *Xenopus* eye development. *Nature* **287**, 850–852 (1980).
65. Eiraku, M. et al. Self-organizing optic-cup morphogenesis in three-dimensional culture. *Nature* **472**, 51–56 (2011).
66. Watanabe, K. et al. Directed differentiation of telencephalic precursors from embryonic stem cells. *Nat. Neurosci.* **8**, 288–296 (2005).
67. Riedl, J. et al. Lifeact: a versatile marker to visualize F-actin. *Nat. Methods* **5**, 605–607 (2008).
68. Yamamoto, H. et al. The apical and basolateral secretion of Wnt11 and Wnt3a in polarized epithelial cells is regulated by different mechanisms. *J. Cell Sci.* **126**, 2931–2943 (2013).
69. O'Brien, L. E., Zegers, M. M. P. & Mostov, K. E. Building epithelial architecture: insights from three-dimensional culture models. *Nat. Rev. Mol. Cell Biol.* **3**, 531–537 (2002).
70. Hasegawa, Y. et al. Emergence of dorsal-ventral polarity in ESC-derived retinal tissue. *Development* **143**, 3895–3906 (2016).
71. Kondrychyn, I. et al. Marcksl1 modulates endothelial cell mechanoresponse to haemodynamic forces to control blood vessel shape and size. *Nat. Commun.* **11**, 5476 (2020).
72. Lin, J. et al. Targeting activated Akt with GDC-0068, a novel selective Akt inhibitor that is efficacious in multiple tumor models. *Clin. Cancer Res.* **19**, 1760–1772 (2013).
73. Sakurai, A., Matsuda, M. & Kiyokawa, E. Activated Ras protein accelerates cell cycle progression to perturb Madin–Darby canine kidney cystogenesis. *J. Biol. Chem.* **287**, 31703–31711 (2012).
74. Harada, K., Negishi, M. & Katoh, H. HGF-induced serine 897 phosphorylation of EphA2 regulates epithelial morphogenesis of MDCK cells in 3D culture. *J. Cell Sci.* **128**, 1912–1921 (2015).
75. Aoki, K. & Matsuda, M. Visualization of small GTPase activity with fluorescence resonance energy transfer-based biosensors. *Nat. Protoc.* **4**, 1623–1631 (2009).

## Acknowledgements

We thank all the members of Okuda's laboratory for discussions; S. Hayashi, Y. C. Wang, and F. Motegi for critical reading; M. Matsuda and K. Okamoto for valuable comments; K. Yoshida for help with experiments; and A. Matsuoka for help with image analysis. This work was supported by the WISE Program for Nano-Precision Medicine, Science, and Technology of Kanazawa University, Ministry of Education, Culture, Sports, Science and Technology (MEXT; to A.T.); the Japan Science and Technology Agency (JST), CREST [Grant Nos. JPMJCR1921 and JPMJCR24B2]; the Japan Agency for Medical Research and Development [AMED; Grant No. 23bm0704065h0003]; the Japan Society for the Promotion of Science (JSPS), KAKENHI [Grants Nos. 21H01209, 21KK0134, 22K18749, 22H05170, 24H01398, and 24H01937]; and the World Premier International Research Center Initiative, MEXT, Japan (to S.O.).

## Author contributions

A.T.: data curation, formal analysis, investigation, methodology, resources, software, validation, visualization, and writing (original draft and revised draft). M.M.: formal analysis and investigation. R.I.: investigation and validation. S.T.: resources and validation. G.S.: resources and validation. S.O.: conceptualization, data curation, formal analysis, funding acquisition, methodology, project administration, resources, software, supervision, visualization, and writing (original draft and revised draft).

## Competing interests

The authors declare no competing interests.

## Additional information

**Supplementary information** The online version contains supplementary material available at <https://doi.org/10.1038/s41467-024-54906-7>.

**Correspondence** and requests for materials should be addressed to Satoru Okuda.

**Peer review information** *Nature Communications* thanks Jonathan Fouchard, and Caren Norden, for their contribution to the peer review of this work. A peer review file is available.

**Reprints and permissions information** is available at <http://www.nature.com/reprints>

**Publisher's note** Springer Nature remains neutral with regard to jurisdictional claims in published maps and institutional affiliations.

**Open Access** This article is licensed under a Creative Commons Attribution-NonCommercial-NoDerivatives 4.0 International License, which permits any non-commercial use, sharing, distribution and reproduction in any medium or format, as long as you give appropriate credit to the original author(s) and the source, provide a link to the Creative Commons licence, and indicate if you modified the licensed material. You do not have permission under this licence to share adapted material derived from this article or parts of it. The images or other third party material in this article are included in the article's Creative Commons licence, unless indicated otherwise in a credit line to the material. If material is not included in the article's Creative Commons licence and your intended use is not permitted by statutory regulation or exceeds the permitted use, you will need to obtain permission directly from the copyright holder. To view a copy of this licence, visit <http://creativecommons.org/licenses/by-nc-nd/4.0/>.

© The Author(s) 2024